Tafreshi, Saeedeh Sarabadani, Moshfegh, Alireza Z.Xaker and De Leeuw, Nora 2019. Mechanism of photocatalytic reduction of CO2 by Ag3PO4(111)/g-C3N4 nanocomposite: A first principles study. Journal of Physical Chemistry C 123 (36) , pp. 22191-22201. 10.1021/acs.jpcc.9b04493

Publishers page: http://dx.doi.org/10.1021/acs.jpcc.9b04493

Mechanism of Photocatalytic Reduction of CO_2 by $Ag_3PO_4(111)/g\text{-}C_3N_4$ Nanocomposite: A First Principles Study

Saeedeh S.Tafreshi,[a,b] **Alireza Z. Moshfegh,**[b,c,*] **Nora H. de Leeuw** [d,*]

[a]*Department of Chemistry, Amirkabir University of Technology, Tehran,15875-4413, Iran* [b]*Department of Physics, Sharif University of Technology, Tehran, 11155-9161, Iran*

[c]*Institute for Nanoscience and Nanotechnology,Sharif University of Technology, Tehran, 14588-8969, Iran* [d]*School of Chemistry, Cardiff University, Main Building, Park Place, Cardiff, CF10 3AT, UK*

Address correspondence to moshfegh@sharif.edu, deleeuwn@cardiff.ac.uk

Abstract

Density functional Theory (DFT) calculations have been performed to investigate the electronic structure and photocatalytic activity of a hybrid $Ag_3PO_4(111)/g\text{-}C_3N_4$ structure. Due to Ag(d) and O(p) states forming the upper part of the valence band and C(p), N(p) and Ag(s) the lower part of the conduction band, the band gap of the hybrid material is reduced from 2.75 eV for $Ag_3PO_4(111)$ and 3.13 eV for monolayer of $g\text{-}C_3N_4$ to about 2.52 eV, enhancing the photocatalytic activity of the $Ag_3PO_4(111)$ surface and $g\text{-}C_3N_4$ sheet in the visible region. We have also investigated possible reaction pathways for photocatalytic CO_2 reduction on the $Ag_3PO_4(111)/g\text{-}C_3N_4$ nanocomposite to determine the most favored adsorption geometries of reaction intermediates and the related reaction energies. For CO_2 reduction, our findings demonstrate that the $Ag_3PO_4(111)/g\text{-}C_3N_4$ heterostructure thermodynamically exhibits a higher selectivity towards CH_4 production than that of CH_3OH. The CO_2 reduction process takes place through either $HCOOH^*$ or $HOCOH^*$ as an intermediate species, where the highest exothermic reaction energy of -2.826 eV belongs to the hydrogenation of t-$COOH^*$ to $HCOOH^*$ and the lowest reaction energy of -0.182 eV for hydrogenations of CH_2O^* to CH_2OH^* and HCO^* to c-$HCOH^*$. Our results from charge density difference calculations of the $Ag_3PO_4(111)/Ag/g\text{-}C_3N_4$ revealed that the charge transfer between the $Ag_3PO_4(111)$ slab and $g\text{-}C_3N_4$ monolayer occurs through mediation of atomic Ag, thus proposing a Z-scheme mechanism. Moreover, a smaller band gap energy of 0.73 eV is calculated for this ternary nanocomposite due to the mid-gap states of the atomic Ag at the interface. These results provide in depth understanding of the reaction mechanism in the reduction and conversion of CO_2 to useful chemicals via an Ag_3PO_4 and g-C_3N_4-based nanocomposite photocatalyst under visible light.

1. Introduction

Population growth and industrial development are among major factors limiting availability of dwindling fossil fuel resources. In addition, as a result of their combustion, CO_2 emissions into the environment and the resulting greenhouse effect have led to significant concerns about climate change.[1] Therefore, conversion of CO_2 to valued products is an important issue in both energy and environmental global concerns. These questions have led to extensive research in CO_2 conversion into useful alternative hydrocarbon products, including methanol (CH_3OH), methane (CH_4), formic acid (HCOOH), and formaldehyde (CH_2O). A number of strategies are considered to address this issue such as photocatalytic reduction of CO_2 using appropriate composite semiconductor photocatalysts.[2-3]

Several photocatalysts have been examined for their potential to catalyze CO_2 conversion reactions, through decreasing their charge carrier recombination rate or via better visible-light harvesting, leading to improved photocatalytic efficiency. Due to the efficient separation of photo-excited electrons and holes, silver orthophosphate (Ag_3PO_4) possesses excellent photocatalytic properties. Recent studies have shown high photo-oxidative capabilities for O_2 evolution from water splitting,[4] as well as decolorization of organic dyes[5] over Ag_3PO_4. The major problem for practical applications of Ag_3PO_4 is its low structural stability. Several studies have been carried out to improve the stability and thus the photocatalytic activity of Ag_3PO_4 by coupling it with other semiconductors, such as TiO_2[6], ZnO[7], Bi_2WO_6[8], BiOI[9], oxidized graphene[10], reduced graphite oxide[11], and carbon quantum dots[12]. Moreover, plasmonic effects induced by Ag nanoparticles generated by Ag_3PO_4, during its coupling with other semiconductor under visible light irradiation, leads to improved charge separation, resulting in a high photocatalytic activity. A comprehensive review on coupling of several 2D materials with a number of semiconductor oxides and the role of interfaces in photocatalytic reactions has been published recently[13].

Graphitic carbon nitride (g-C_3N_4) has been reported as a novel, metal-free layered semiconductor and visible-light-driven photocatalyst for the degradation of organic pollutants[14] and hydrogen evolution from water splitting,[15] as well as CO_2 reduction[16]. Due to its medium band gap energy (~2.7 eV), low specific surface area and fast charge recombination rate, it is widely accepted that g-C_3N_4 must be coupled with other photocatalysts to enhance its photocatalytic activity, including TiO_2[17], CdS[18], SiO_2[19], Al_2O_3[20] or Ag_3VO_4[21]. In addition, the photocatalytic activity of g-C_3N_4 can be also improved by doping it with other elements, e.g. B/P [22], Na[23], K[23] or Au[24].

A few studies have focused on combining Ag_3PO_4 with g-C_3N_4 to enhance the photocatalytic activity. For example, a higher photocatalytic activity in water oxidation and oxygen production for the Ag_3PO_4/g-C_3N_4 nanocomposite was found with a Z-scheme charge transfer mechanism, where Ag atoms generated by Ag_3PO_4 act as a cross-linking bridge the interface of the Ag_3PO_4 and g-C_3N_4.[25-26] Other studies have also demonstrated enhanced photocatalytic performance of the Ag_3PO_4/g-C_3N_4 system towards decomposition of Methyl Orange[27], phenol[28], bisphenol A[28], Rhodamine B[29], ciprofloxacin[30], and the oxidation of ethylene[31] under visible light. A higher photocatalytic performance of combined Ag_3PO_4 and g-C_3N_4 towards degradation of methylene blue [30, 32-33] and removal of NO[33] was also studied, where the enhancement was ascribed to the efficient separation of electron-hole pairs through a Z-scheme charge transfer mechanism of the

$Ag_3PO_4/Ag/g\text{-}C_3N_4$. Zhang et al.[34] have reported improvement of the stability and light absorption ability of the $Ag_3PO_4/g\text{-}C_3N_4$ compared to pure Ag_3PO_4, where they measured enhancement in photodegradation of diclofenac for the hybrid system. In another study, the $Ag_3PO_4/g\text{-}C_3N_4$ nanocomposite was synthesized by Zhou et al.[35] They showed a higher photocatalytic activity towards the degradation of sulfamethoxazole through a Z-scheme charge transfer mechanism. Yiming He et al.[36] have synthesized the $Ag_3PO_4/g\text{-}C_3N_4$ heterojunction using a simple in situ deposition method, observing enhanced photocatalytic CO_2 reduction, where atomic Ag acted as the recombination center for electrons and holes by a Z-scheme charge carrier pathway.

However, despite these promising studies, to the best of our knowledge, no computational study has as yet been carried out on the $Ag_3PO_4/g\text{-}C_3N_4$ hybrid system. In this investigation, geometrical and electronic properties of the $Ag_3PO_4(111)/g\text{-}C_3N_4$ heterojunction photocatalyst for CO_2 photo-reduction have been studied using density functional theory (DFT) calculations, to gain understanding of the charge transfer mechanism at the interface.

As shown in theoretical and experimental studies, control of surface structure is an important requirement for the improvement of the photocatalytic activity, where it is widely accepted that a high surface energy – indicating a less stable and more reactive surface - is beneficial to improve the photocatalytic efficiency of the facets[33, 37-39]. It is well known that {111} facet of the Ag_3PO_4 is the least stable and most reactive facet with its higher surface energy among the {111}, {110} and {100} facets[33, 37-38]. The literature also indicates that the exposed {111} facets show the highest photocatalytic activity under visible light irradiation among the lowest-index {111}, {110} and {100} facets, due to the larger band gap of the Ag_3PO_4 {111} surface which suppresses the recombination of electron–hole pairs, in addition to the photo-generation of electrons with higher energy and activity in the conduction band of {111} surfaces than those on the other low-index surfaces.[33]

Furthermore, a hybrid g-C_3N_4/Ag_3PO_4 material with reactive {111} facets is expected to display excellent photocatalytic performance under visible light irradiation, as confirmed by experiment.[33, 38]. Thus in this study, the Ag_3PO_4(111) was chosen to be coupled with a monolayer of g-C_3N_4, where a DFT approach was used to define the effect of metallic Ag as a recombination center on the electronic properties of the hybrid Ag_3PO_4(111)/g-C_3N_4 photocatalyst in the CO_2 reduction process.

2. Computational Details

We have performed electronic structure calculations using DFT as implemented in the Vienna Ab initio Simulation Package (VASP)[40-41]. The total energy calculations have been performed using the Perdew-Burke-Ernzerhof (PBE)[42] form of the generalized gradient approximation (GGA) with the projector augmented wave (PAW) method[43-45]. As has been shown in other studies[45], inclusion of the long-range Van der Waals (vdW) forces improves the energy description of each system, and we have therefore employed the DFT-D3, method of Grimme as implemented in VASP[46].

In this study, the Ag_3PO_4(111)/g-C_3N_4 nanocomposite was created by adding a monolayer of g-C_3N_4 on top of a Ag_3PO_4(111) slab. Since experiment has shown that Ag^+ generated by Ag_3PO_4 is reduced to Ag atom and the composite consists of Ag_3PO_4, Ag and g-C_3N_4, we investigated the effect of atomic Ag in the composite on the photocatalytic activity of the Ag_3PO_4(111)/g-C_3N_4 hetero-structure. To create the Ag_3PO_4(111)/Ag/g-C_3N_4 composite, we first added an Ag ad-atom to the g-C_3N_4 and allowed this structure to relax. We next positioned this material with the Ag side on top of the Ag_3PO_4(111) slab and optimized the entire slab. The hybrid photocatalyst structure has a hexagonal super cell with dimension of 8.287Å and a lattice mismatch of nearly 6% (see Figure 1).

The electron wave functions were expanded using plane waves with a cutoff energy of 600 eV for g-C_3N_4 bulk and monolayer and 450 eV for Ag_3PO_4 bulk, Ag_3PO_4(111), Ag_3PO_4(111)/g-C_3N_4 and Ag_3PO_4(111)/Ag/g-C_3N_4 structures, which high values ensured that no Pulay stresses occurred within the cells during relaxation. The convergence criteria for the residual force and energy on each atom during structure relaxations were set to 0.01 eV/Å and 10^{-5} eV, respectively. A vacuum space was set more than 20 Å that is introduced to avoid interactions between periodic images.

Hybrid DFT, which is obtained by mixing in a fixed amount of Hartree–Fock exchange, was used to get exact electronic properties.[47] PBE0[48] and Heyd-Scuseria-Ernzerhof (HSE0)[49] formalisms were applied for Ag_3PO_4(111) and g-C_3N_4, respectively to obtain the correct band gap in line with [5, 12, 50-53] the literature. In addition, PBE0 used for the hybrid Ag_3PO_4(111)/g-C_3N_4 and ternary Ag_3PO_4(111)/Ag/g-C_3N_4 nanocomposites, because this hybrid functional leads to band gaps in the visible light irradiation area that matches other studies.[25-36] A 6×6×1 gamma grid[54] of k-points was used to sample the Brillouin zone for monolayer g-C_3N_4 and a 4×4×1 grid for the Ag_3PO_4(111) slab, Ag_3PO_4(111)/g-C_3N_4 and Ag_3PO_4(111)/Ag/g-C_3N_4 hybrid structures. The g-C_3N_4 monolayer modeled by a $(\sqrt{3} \times \sqrt{3})$ 30° supercell, which is equivalent to a 3 × 3 supercell containing 21 atoms and three primitive unit cells as has been used in the study by Algara et al.[55] sits on a 1 × 1 Ag_3PO_4(111) surface slab containing 80 atoms and six $_4{}^{-3}$ units, including four bottom $_4{}^{-3}$ units fixed at bulk position.

3. Results and Discussion

3.1. Geometrical Structure

We have investigated the Ag_3PO_4 bulk, $Ag_3PO_4(111)$ surface, g-C_3N_4 bulk and g-C_3N_4 monolayer. The optimized cell parameters were = = = 6.012 Å for Ag_3PO_4 bulk and = = 4.746 Å

for a monolayer of g-C_3N_4, which are both in good agreement with measured experimental values (6.004 Å[56] for Ag_3PO_4 bulk and 4.742 Å [57] for g-C_3N_4 monolayer) and previous theoretical values (6.010 Å[58] for Ag_3PO_4 bulk and 4.774 Å [50] for g-C_3N_4 monolayer).

The thermodynamic stability of the $Ag_3PO_4(111)$/g-C_3N_4 nanocomposites can be described by the interface adhesion energy using the following equation:

$$= \quad {}_{4(111)}/ \; {}_{-\,3\,4} - \quad {}_{3} \quad {}_{4(111)} - \quad {}_{-\,3\,4}$$

where ${}_{3}$ ${}_{4(111)}/$ ${}_{-\ 3\ 4}$’ ${}_{3}$ ${}_{4(111)}$ and ${}_{-\ 3\ 4}$ represent the total energy of the $Ag_3PO_4(111)$/g-C_3N_4 hybrid structure, the $Ag_3PO_4(111)$ surface, and the g-C_3N_4 monolayer, respectively. The is calculated at about -1.90 eV for the ${}_{3}$ ${}_{4(111)}$ $/{}_{-\,3\,4}$. The negative denotes that the hybrid structure is stable thermodynamically with respect to the individual component materials and that strong interactions exists between the g-C_3N_4 monolayer and $Ag_3PO_4(111)$ surface.

The top and side views of the $Ag_3PO_4(111)$/g-C_3N_4 and $Ag_3PO_4(111)$/Ag/g-C_3N_4 interface models used in our calculations, after geometry optimization, are shown in Fig. 1, indicating more interaction at the interface of the ternary composite. There is a shorter distance between g-C_3N_4 layer and $Ag_3PO_4(111)$ surface in the Ag_3PO_4/Ag/g-C_3N_4 and a more distorted g-C_3N_4 structure (Fig. 1b), due to the presence of atomic Ag at the interface..

To investigate the charge transfer mechanism between g-C_3N_4 and the $Ag_3PO_4(111)$ surface, the differential charge densities are calculated and plotted in Fig. 2. It can be seen that more charge transfer occurs between the Ag atom and the g-C_3N_4 monolayer, leading to more interaction at the interface; experiment has already confirmed that Ag acts as a recombination center at the interface, leading to improvement in the photocatalytic activity[36].

3.2. Band Structure and Density of States

To understand the nature of the interaction between g-C_3N_4 monolayer and Ag_3PO_4(111) surface, band structure calculations of the g-C_3N_4 monolayer, Ag_3PO_4(111) surface, and Ag_3PO_4(111)/g-C_3N_4 hybrid structure, as well as the g-C_3N_4 and Ag_3PO_4 bulk, were carried out and the results are shown in Figure 3. The calculated results with PBE0 hybrid functional show that Ag_3PO_4 bulk has an indirect band gap of 2.47 eV, with the valence band maximum (VBM) located at M point and the conduction band minimum (CBM) placed at the Γ point (Fig. 3a), which agrees well with other experimental[5] and theoretical studies[51]. The Ag_3PO_4(111) surface has a direct band gap of 2.75 eV, shown in Fig. 3b, which matches the theoretical result reported by Zheng et al.[12]. In addition, the direct band gaps for g-C_3N_4 bulk and its monolayer, calculated with the HSE0 hybrid functional, are 2.75 and 3.13 eV at X and Y high symmetry points, (Fig. 3c and 3d), respectively. These results are also consistent with recent experimental and calculated findings [50, 52-53]. The calculated band structure of the hybrid Ag_3PO_4(111)/g-C_3N_4 system, with an indirect band gap as large as 2.52 eV, is illustrated in Fig. 3e. It should be noted that the obtained smaller band gap of the hybrid structure can dramatically enhance the photocatalytic performance of g-C_3N_4 monolayers under visible irradiation.

To further understand the electronic structure at the interface of the Ag_3PO_4(111)/g-C_3N_4 hybrid system, the total DOS (TDOS) and its projected DOS (PDOS) were also calculated and the results are shown in Figure 4. According to Fig. 4a, while the CBM of the Ag_3PO_4(111)/g-C_3N_4 hetero-structure mainly originates from the atomic orbitals of the g-C_3N_4 sheet, the VBM is dominated by the Ag_3PO_4(111) states. The VBM of the hetero-structure is mainly occupied by the O(p) and

Ag(d) orbitals of the Ag_3PO_4(111), where they are higher than those of g-C_3N_4 (Fig. 4b). Moreover, Fig. 4c indicates that the CBM of the Ag_3PO_4(111)/g-C_3N_4 is composed of the C(p) and N(p) orbitals of g-C_3N_4 monolayer, with the Ag(s) and O(p) orbitals of the Ag_3PO_4(111) also occupying some states of CBM.

To examine the effect of atomic Ag on the electronic properties of the interface, we have further investigated the total density of states and band structure of the Ag_3PO_4/Ag/g-C_3N_4 composite, as shown in Fig. 5. The presence of atomic Ag at the interface between the Ag_3PO_4(111) surface and g-C_3N_4 monolayer is confirmed by the states in the mid-gap of the Ag_3PO_4/Ag/g-C_3N_4 hybrid structure near the VBM, where they act as a recombination charge center (Fig. 5a). These states has decreased the band gap to 0.73 eV where the VBM is located at the T point, and CBM appears at the Γ point, resulting in an indirect band gap semiconductor (Fig. 5b). To gain better understanding of the mid-gap states, we investigated the PDOS of the Ag_3PO_4/Ag/g-C_3N_4 structure, as shown in Fig. 6. Our calculations reveal that the main contributors to the mid-gap states are the atomic Ag at the interface, as well as the O atoms in the top layer of Ag_3PO_4 and the closest N and C atoms of the g-C_3N_4 sheet. These results confirm that the Ag atoms are generated via the reduction of ionic Ag of the Ag_3PO_4(111)/g-C_3N_4 composite; their presence has recently been confirmed by experiment.[36] The above findings indicate that the Ag_3PO_4(111)/g-C_3N_4 system is a Z-scheme type photo-catalyst, which has already been reported by experiment[36, 59]. It is worth noting that the formation of Ag atoms in the composite, acting as charge carrier recombination centers, thus promotes the separation efficiency of electron-hole pairs, leading to higher photo-activity of Ag_3PO_4/g-C_3N_4[60-61].

In general, The VBM and CBM edge positions of a semiconductor can be calculated according to the following equations;

$$= - \qquad + 0.5$$

$$= \qquad -$$

where χ is the absolute electronegativity of the semiconductor, which for g-C_3N_4 and Ag_3PO_4 are 4.73 and 5.96 eV, respectively. represents the energy of free electrons in the normal hydrogen electrode (NHE) (about 4.5 eV), is the band gap energy of the semiconductor. The calculated band gaps for the g-C_3N_4 monolayer, Ag_3PO_4 (111) surface and Ag_3PO_4/g-C_3N_4 hybrid composite are 3.13, 2.75 and 2.52 eV, respectively. According to the above equations, the positions of the CB and VB of g-C_3N_4 are then -1.34 and 1.80 eV versus NHE, as shown in Fig. 7, which the obtained values are consistent with other studies[50]. As displayed in Fig. 7, the calculated CB and VB for the Ag_3PO_4(111) surface are 0.09 and 2.84 eV, versus NHE, respectively.

Ag_3PO_4 (111) with a band gap of 2.75 eV can absorb visible light, but its CB edge is located at 0.09 V, which is lower than the potential required for reduction of CO_2 to hydrocarbon products like CH_3OH, CH_4, HCOOH and CH_2O, (see Fig. 7). In contrast, the CB of g-C_3N_4 is above the CO_2 reduction reaction potentials and the photo-generated electrons can thus easily reduce CO_2 to these products (Fig. 7). As such, the hybrid Ag_3PO_4(111)/g-C_3N_4 system can catalyze the CO_2 reduction only if it follows the Z-scheme mechanism, which could happen through the presence of atomic Ag as the recombination center for the photo-generated electrons in the CB of Ag_3PO_4(111) and holes in the VB of the g-C_3N_4 sheet, as displayed in Fig. 7. Considering such a mechanism, the photo-excited electrons in the CB of g-C_3N_4 can reduce CO_2, leading to excellent photo-catalytic activity of the Ag_3PO_4(111)/g-C_3N_4 hetero-structure in CO_2 photo-reduction processes. These results are also supported by experimental findings[36]. The mechanisms of CO_2 reduction are discussed in further details in the following section.

3.3. Mechanisms of CO_2 Reduction

Upon photo-irradiation of the photo-catalyst, photo-generated electrons ($^{-}$) will be transferred to the conduction band of g-C_3N_4 and Ag_3PO_4(111), leaving holes (h^{+}) in the valence band of these semiconductors to catalyze the water oxidation to form the hydrogen source ($^{+}$) required for the CO_2 reduction, according to the following reactions:

$- \ 3 \ 4+h \rightarrow {}^{-}(\qquad)+h^{+}(\quad)$
$_{3} \qquad {}_{4}+h \rightarrow {}^{-}(\qquad)+h^{+}(\qquad)$
$2_{2} \qquad +4h^{+}\rightarrow {}_{2}+4 \qquad {}^{+}$

The overall reactions of CO_2 reduction to form HCOOH, CH_2O, CH_3OH and CH_4 using 2, 4, 6 and 8 electrons in the presence of hydrogen are expressed as follows:

$_{2}+2 \qquad {}^{+}+2\,{}^{-}\rightarrow$
$_{2}+4 \qquad {}^{+}+4\,{}^{-}\rightarrow \ {}_{2}+{}_{2}$
$_{2}+6 \qquad {}^{+}+6\,{}^{-}\rightarrow \ {}_{3} \qquad + \qquad {}_{2}$
$_{2}+8 \qquad {}^{+}+8\,{}^{-}\rightarrow \ {}_{4}+2\,{}_{2}$

The overall reactions above include several elementary hydrogenation steps, which are determined by the most stable product at each step, as shown in Fig.8; where reaction energies of all elementary steps are listed in Table 1.

The most favorable adsorption geometries of all intermediates are shown in Fig. 9. The initial step of CO_2 hydrogenation is the formation of the formate ($HCOO^{*}$) or the carboxyl species (trans-$COOH^{*}$ and/or cis-$COOH^{*}$)[62]. The formate species prefer to adsorb perpendicularly, with two O atoms pointing towards the surface, with short O N distances of 2.879 and 3.012 Å, as shown in

Fig. 9. The calculated reaction energy of hydrogenation of CO_2 to HCOO (${}_{2}^{*}+{}^{+*}\rightarrow \qquad {}^{*}$) is -1.565 eV, i.e. an exothermic reaction, see Table 1. The adsorbed CO_2 could also be

hydrogenated to a carboxyl group with two cis and trans conformers (Fig. 9) $_2{}^* + {}^+{}^* + {}^- \rightarrow , - {}^*$, which reactions are also exothermic with energies of -1.983 eV and -1.014 eV for the cis and trans conformer, respectively. As the cis conformer is more stable on the $Ag_3PO_4(111)/g\text{-}C_3N_4$ hetero-structure, it could possibly be the most abundant intermediate after the first step of CO_2 hydrogenation. While cis-COOH adsorbs through its carbon atom at a distance of 1.589 Å from the carbon atom of the $g\text{-}C_3N_4$ monolayer, trans-COOH points perpendicularly towards the surface through its oxygen atom, as shown in Fig. 9.

Subsequent hydrogenation products of formate and carboxyl species are formic acid ($HCOOH^*$) and dihydroxycarbene (cis-cis, cis-trans and trans-trans $HOCOH^*$). Dihydroxycarbene adsorbs in different configurations due to cis and trans structures on either side of the C O bond, as shown in Fig. 9. The corresponding elementary reactions of this step are $^* + {}^+{}^* + {}^- \rightarrow$ * , , − $^* + {}^+{}^*$ and , − $^* + {}^+{}^*$ $\rightarrow$, , $- {}^*$. As shown in Table. 1, the hydrogenation step of formate to formic acid is significantly exothermic on the $Ag_3PO_4(111)/g\text{-}C_3N_4$ with a reaction energy of -2.275 eV. Formation of formic acid through hydrogenation of the trans carboxyl group is even more exothermic with a reaction energy of -2.826 eV. The calculated reaction energies of hydrogenation of trans and cis carboxyl leading to the production of different conformers of $HOCOH^*$ show that the tt-$HOCOH^*$ conformer is most likely to be formed. As shown in Table. 1, transformation of cc-HOCOH and ct-HOCOH to tt-HOCOH via reactions of $- {}^* \rightarrow - {}^*$ and $- {}^* \rightarrow - {}^*$ are exothermic by -0.484 eV and -0.026 eV, respectively. As Fig. 9 shows, formic acid points towards the N atom of the $g\text{-}C_3N_4$ surface through the H atom of its OH group with an H N bond length of 1.865 Å. While the t,t isomer of $HOCOH^*$ bonds to C atom of the surface through its carbon atom with bond length of 1.558 Å, the two other conformers, c, t and c,c $HOCOH^{*}$, point toward the surface with their hydrogen atom at distances of 1.657 and 1.846 Å, respectively. As to the produced intermediates, four possible paths leading to CH_3OH and CH_4 formation through either $HCOOH^{*}$ or $HOCOH^{*}$ were studied in detail, as shown in Figure 10.

3.3.1. The reaction pathways of CO_2 to CH_3OH or CH_4 through $HCOOH^{*}$

The reaction energy profiles of the different potential pathways are shown in Fig. 10. Produced $HCOOH^{*}$ is less likely to desorb from the surface as this process would be endothermic requiring an energy of 4.532 eV. Subsequent hydrogenation of the produced $HCOOH^{*}$ intermediate can result in the formation of either hydroxymethoxy (H_2COOH^{*}) via $^{*} + {}^{+} {}^{*}$ * , an endothermic reaction (1.898 eV), or a dissociation reaction into formyl (HCO^{*}) and OH^{*} via $^{*} \rightarrow$ $^{*} + {}^{*}$ with an exothermic reaction energy of -1.250 eV. Therefore, $^{+ - \rightarrow 2}$ formation of H_2COOH^{*} is less likely to happen due to its high reaction energy, but if formed it points to an N atom of the surface via one of its H atoms at a distance of 1.852 Å, (see Fig. 9). The most likely path after the formation of $HCOOH^{*}$ involves its dissociation to HCO^{*}, where the carbon atom of HCO^{*} binds closely to the N atom of the surface with a bond length of 1.409 Å, (Fig. 9).

Further hydrogenation of HCO^{*} can lead to the formation of either formaldehyde (CH_2O^{*}), via $^{*} + {}^{+} {}^{*} + {}^{-} \rightarrow \; {}_{2} {}^{*}$ with an exothermic reaction energy of -0.930 eV, or cis-$HCOH^{*}$ and trans-$HCOH^{*}$, via $^{*} + {}^{+} {}^{*} + {}^{-} \rightarrow \; - {}^{*}$ and $^{*} + {}^{+} {}^{*} + {}^{-} \rightarrow \; - {}^{*}$ with reaction energies of -0.182 and -0.884 eV, respectively. While the latter species adsorbs perpendicularly on the surface, it prefers to bridge two N atoms of g-C_3N_4 through its C atom with C N bond lengths of 1.465 and 1.524 Å. The carbon atom of cis-HCOH also prefers to bridge C and N atoms of the g-C_3N_4 layer with bond lengths of 1.570 and 1.599 Å. Transformation of c-

$HCOH^{*}$ to t-$HCOH^{*}$ is favorable energetically, with an exothermic reaction energy of -0.702 eV. Therefore, further hydrogenation can be continued from t-$HCOH^{*}$ to CH_2OH^{*} by the reaction of $-{}^{*}+{}^{*}{}^{+}+{}^{-}\rightarrow \; {}_{2}{}^{*}$ releasing an energy of 0.228 eV. The produced CH_2O^{*} from HCO^{*} hydrogenation prefers to lie almost parallel on the surface with the closest distance of 3.492 Å between its carbon atom and the nitrogen of the g-C_3N_4 monolayer. A large distance between molecule and hybrid structure, in addition to the unchanged geometry after adsorption, shows that formaldehyde adsorbs physically on the hybrid Ag_3PO_4/g-C_3N_4 system (Fig. 9).

Further hydrogenation of CH_2O^{*} results in the formation of hydroxymethyl (CH_2OH^{*}) or a methoxy species (CH_3O^{*}), with exothermic energies of -0.182 and -1.216 eV via reactions of $_{2}$ ${}^{*}+ \quad {}^{+*}+{}^{-}\rightarrow \; {}_{2}$ *and $_{2}$ ${}^{*}+{}^{+*}+{}^{-}\rightarrow \; {}_{3}$ *, respectively. As Fig. 9 shows, both the CH_2OH^{*} and CH_3O^{*} intermediates bond to the carbon of the g-C_3N_4 monolayer of the hybrid structure, with a C C distance of 1.580 Å and C O distance of 1.397 Å, respectively.

CH_3O^{*} and CH_2OH^{*} can also hydrogenate to form methanol CH_3OH^{*} via ${}_{3}{}^{*}+{}^{+*}+{}^{-}\rightarrow \; {}_{3}{}^{*}$ and ${}_{2}{}^{*}+{}^{+*}+{}^{-}\rightarrow \; {}_{3}{}^{*}$ where both reactions are exothermic with reaction energies of -0.419 and -1.453 eV, respectively. The methanol molecule points to the surface by its OH group, where the distance between its H atom and the closest nitrogen atom of the surface is 3.007 Å, (Fig. 9). Thus, methanol production from CO_2 reduction via HCOOH on the $Ag_3PO_4^{*}$(111)/g-C_3N_4 involves a sequence of elementary steps, as shown below:

$$2^{*}\rightarrow \quad {}^{*},\;,\; -\,{}^{*}\rightarrow \quad {}^{*}\rightarrow \quad {}^{*}\rightarrow \,,\, -\,{}^{*},2\,{}^{*}\rightarrow \; 2\,{}^{*},3\,{}^{*}\rightarrow \; 3\,{}^{*}$$

It should be noted that the largest exothermic reaction energy of -2.826 eV occurs during the hydrogenation of t-$COOH^{*}$ to $HCOOH^{*}$ and the smallest reaction energy of -0.182 eV occurs in the hydrogenations of CH_2O^{*} to CH_2OH^{*} and HCO^{*} to c-$HCOH^{*}$.

Dissociation of CH_2OH^* to CH_2^* (${}_2 \quad {}^* \rightarrow \; {}_2{}^* + \quad {}^*$) with an exothermic reaction energy of -2.510 eV is another likely reaction, which leads to methane (CH_4) production via subsequent hydrogenations of CH_2^* and CH_3^*, through ${}_2{}^* + {}^+{}^* + {}^- \rightarrow \; {}_3{}^*$ and ${}_3{}^* + {}^+{}^* + {}^- \rightarrow \; {}_4{}^*$ reactions, respectively. These reactions are both likely to happen as they are highly exothermic with reaction energies of -1.141 and -1.508 eV. While the carbon of CH_2^* prefers to bond to the nitrogen of g-C_3N_4 with a bond length of 1.326 Å, CH_3^* adsorbs on top of the carbon atom of g-C_3N_4 layer with C C bond length of 1.594 Å, and CH_4^* interacts through one of its H atoms at a distance of 2.929 Å from the N atom of g-C_3N_4. Similarly, the sequence of elementary steps for CH_4 production through HCOOH species is as follow:

$${}_2{}^* \rightarrow \quad {}^*, \;, \; - {}^* \rightarrow \quad {}^* \rightarrow \quad {}^* \rightarrow , \; - {}^*, 2\,{}^* \rightarrow \; {}_2\,{}^* \rightarrow \; {}_2{}^* \rightarrow \; {}_3{}^* \rightarrow \; {}_4{}^*$$

In this sequence, the largest exothermic reaction energy of -2.826 eV occurs in the hydrogenation of t-$COOH^*$ to $HCOOH^*$ and the smallest reaction energy of -0.182 eV corresponds to CH_2OH^* and c-$HCOH^*$ production from CH_2O^* and HCO^*, respectively.

3.3.2. The reaction pathways of CO_2 to CH_3OH or CH_4 through HOCOH

The reaction energy profiles of the pathways are shown in Fig. 10. As discussed before, tt-HOCOH is the most favored conformer of HOCOH whose dissociation leads to formation of COH^* via $- {}^* \rightarrow \quad {}^* + {}^*$ which is an exothermic reaction by -2.097 eV. COH^* binds through its carbon atom to three nitrogen atoms of g-C_3N_4 with C N bond lengths of 1.439, 1.460 and 1.487 Å. Further hydrogenation of COH^* to $HCOH^*$ is also exothermic for both cis-$HCOH^*$ and trans-$HCOH^*$ by -1.114 and -1.816 eV, respectively. Similar to the mechanism through $HCOOH^*$ (discussed in section 3.3.1), further hydrogenation of HCOH* results in production of CH_2OH^* and CH_3OH^*. Produced CH_2^* from the dissociation of CH_2OH^* leads to final products of

CH_3^* and CH_4^*. In summary, the following paths are involved in the production of CH_3OH^* and CH_4^* via $HOCOH^*$, respectively;

$$_{2}{}^{*}\rightarrow \ , \ - \qquad {}^{*}\rightarrow \ - \qquad {}^{*}\rightarrow \ {}^{*}\rightarrow \ - \ {}^{*}\rightarrow \ _{2} \qquad {}^{*}\rightarrow \ _{3} \qquad {}^{*}$$

$$2^{*}\rightarrow \ , \ - \qquad {}^{*}\rightarrow \ - \qquad {}^{*}\rightarrow \ {}^{*}\rightarrow \ - \ {}^{*}\rightarrow \ 2 \qquad {}^{*}\rightarrow \ 2^{*}\rightarrow \ 3^{*}\rightarrow \ 4^{*}$$

While the smallest reaction energy for both paths through $HOCOH^*$ relates to the hydrogenation reaction of t- $HCOH^*$ to CH_2OH^* (-0.228 eV), the largest reaction energies for methanol and methane production pathways correspond to the dissociation reactions of tt-$HOCOH^*$ and CH_2OH^*, with energies of -2.097 and -2.511 eV, respectively.

Desorption of produced CH_3OH^*, $HCOOH^*$, CH_2O^* and CH_4^* needs more energy due to their highly endothermic desorption energies of 4.544, 4.532, 4.235 and 4.213 eV, respectively. Surface coverage of these species; surface hydration; surface reconstruction; and/or increasing the temperature could all reduce the desorption energies to add desorption of the product species [63]. Temperature Programmed Desorption (TPD) could provide further insight into the temperature-dependence of desorption and show the temperatures at which desorption of the relevant species would occur, which could then feed back into mechanistic pathway calculations.

Considering the mechanisms described above and shown in Fig. 10, since CH_4 formation is an exothermic reaction releasing as much as 2.43 eV compared to 1.18 eV for the production of CH_3OH, CH_4 formation is likely to be the most favored pathway on the hybrid Ag_3PO_4(111)/g-C_3N_4, via either $HCOOH^*$ or $HOCOH^*$ intermediates, which are both likely to happen thermodynamically. We have also calculated the energetics of a few reactions on the Ag_3PO_4(111)/Ag/g-C_3N_4 to see if the presence of the Ag affects the energetics of the reactions and/or the adsorption geometries and energies. However, we did not find any significant changes in the reaction energetics results when the composite includes Ag. A kinetic study determining the reaction barriers could provide further insight into the reaction pathways of CO_2 reduction on the $Ag_3PO_4(111)/g\text{-}C_3N_4$ hetero-structure.

4. Conclusions

DFT calculations have been employed to study the hybrid $Ag_3PO_4(111)/g\text{-}C_3N_4$ system as a potential (photo-)catalyst in the reduction of CO_2. The band gap of the hybrid structure is reduced to 2.52 eV, improving the photocatalytic capability of the $Ag_3PO_4(111)$ surface and $g\text{-}C_3N_4$ monolayer under visible light. We have further investigated the mechanism of CO_2 reduction to possible hydrocarbons, catalyzed by the hybrid system, where our calculated reaction energies revealed that the production of CH_4 is the dominant pathway through either $HCOOH^*$ or $HOCOH^*$ as intermediates. It was found that the largest exothermic reaction energy of -2.826 eV produced during the hydrogenation of $t\text{-}COOH^*$ to $HCOOH^*$ and the smallest reaction energy of -0.182 eV for the hydrogenations of CH_2O^* to CH_2OH^* and HCO^* to $c\text{-}HCOH^*$.

Our electronic structure calculations of the ternary $Ag_3PO_4(111)/Ag/g\text{-}C_3N_4$ nanocomposite revealed that the Ag atom at the interface of $Ag_3PO_4(111)$ and $g\text{-}C_3N_4$ act as a charge recombination center where the charge transfer occurs, promoting the electron-hole separation in the hybrid $Ag_3PO_4(111)/g\text{-}C_3N_4$ system through a Z-scheme mechanism, leading to a highly efficient photo-catalyst, as has been seen in experiment. The band structure calculation of the ternary composite confirms the presence of mid-gap states of the atomic Ag at the interface, leading to a smaller band gap and more efficient Z-scheme photo-catalyst.

This study has investigated the fundamental electronic properties of a highly efficient visible light-active photo-catalysts and its activity towards CO_2 reduction from a thermodynamic point of view.

A further kinetic study will provide better understanding of the mechanism of CO_2 reduction on the $Ag_3PO_4(111)/g\text{-}C_3N_4$ hybrid structure. Furthermore, doped $g\text{-}C_3N_4$ coupled with $Ag_3PO_4(111)$ has also been suggested experimentally and theoretical studies may help to identify the effects of different dopants on the photo-catalytic activity of the hybrid structure. Finally, other low-index surfaces of Ag_3PO_4 such as {100} could also be investigated as interfaces to be coupled with $g\text{-}C_3N_4$ to see if and how this would affect the photo-catalytic activity of the reaction under similar conditions.

Acknowledgements

The authors would like to thank the Research and Technology Council of Sharif University of Technology for financial assistance. SST acknowledges the Iran's National Elites Foundation (INEF) for support of the project. AZM thanks INSF through the Chair of Surface/Interface Project (940009) for financial assistance. The invaluable discussions with Hamid Mehdipoor are also acknowledged. This work has used computational facilities of the Advanced Research Computing @ Cardiff (ARCCA) Division, Cardiff University, UK.

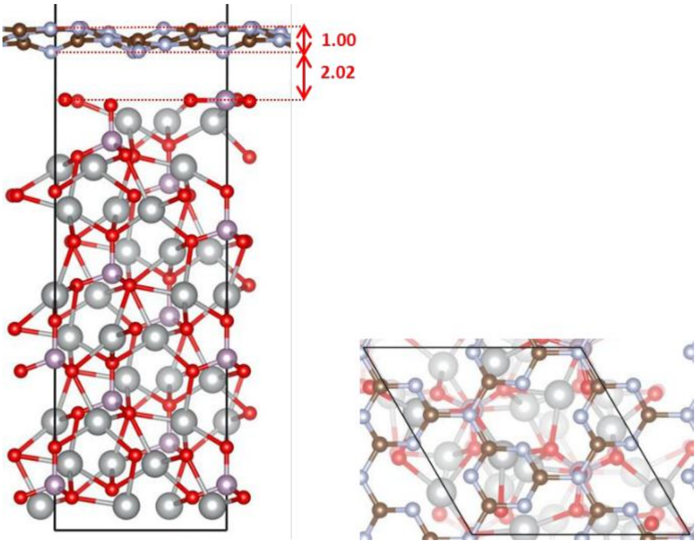

a)

)

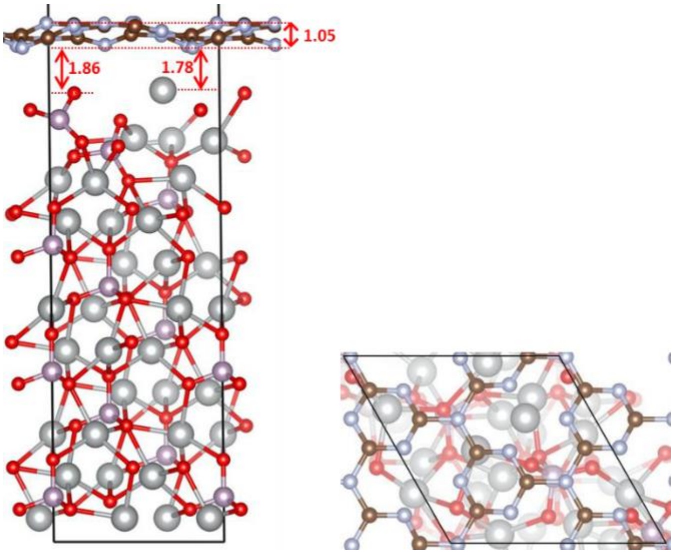

b)

Fig. 1. Top and side geometries of a) Ag_3PO_4/g-C_3N_4 and b) Ag_3PO_4/Ag/g-C_3N_4 interface, after optimization. Colors of Ag, P, O, N and C atoms are silver, purple, red, blue and brown, respectively. All values are in Angestrom.

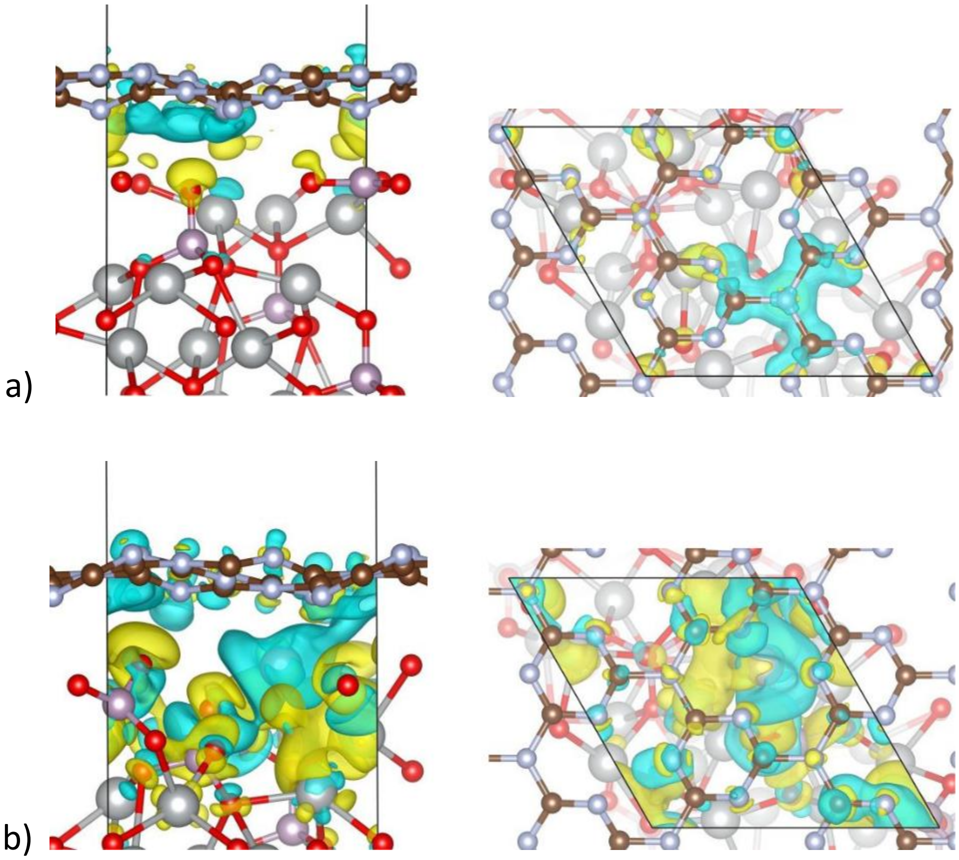

Fig. 2. Charge density difference of nanocompositions of (a) Ag_3PO_4(111)/g-C_3N_4, (b) Ag_3PO_4(111)/Ag/g-C_3N_4 by an iso-surface of ± 0.001 e/$Å^3$, where yellow and blue colors denote lost and gain of electron density.

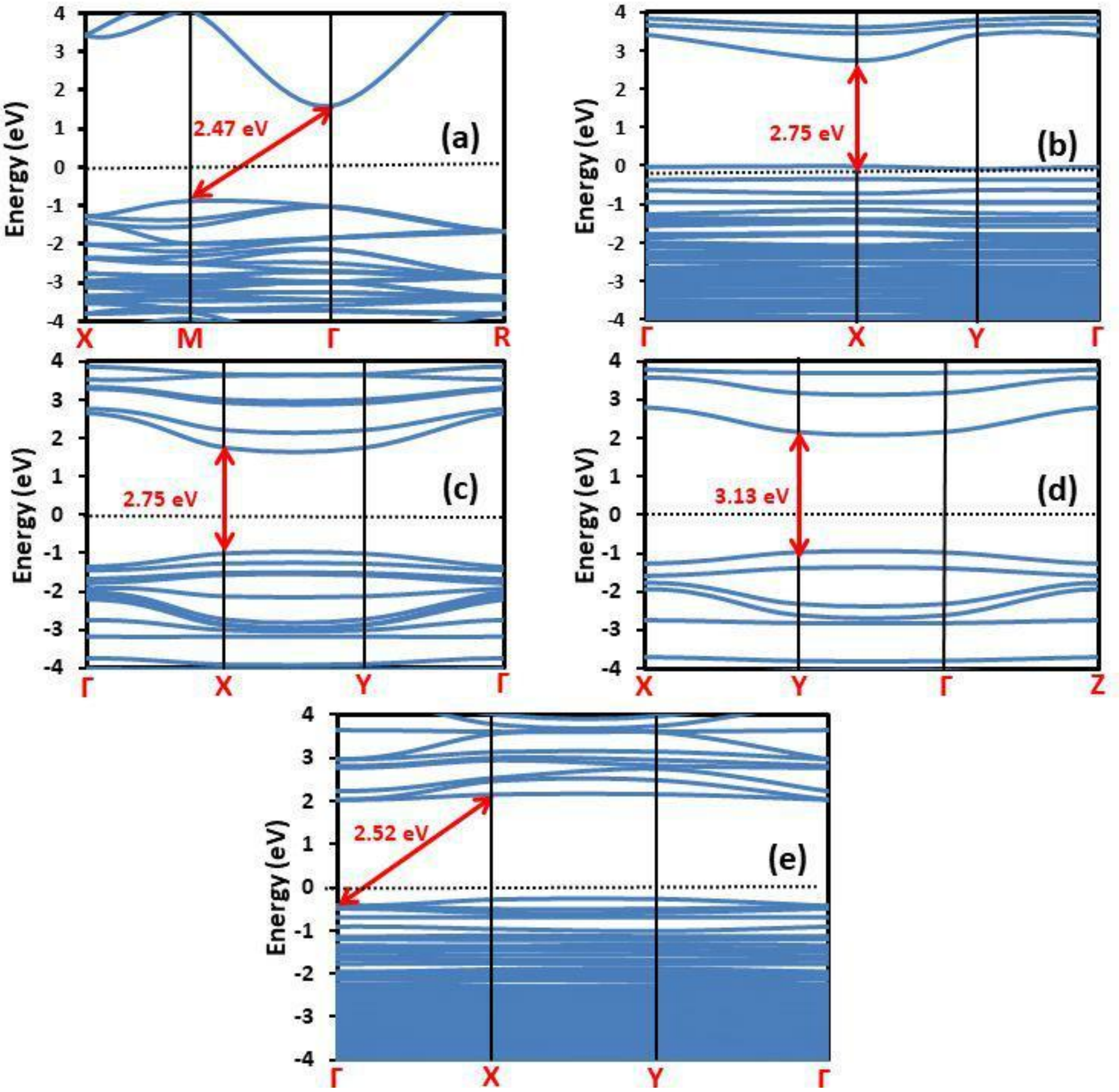

Fig. 3. The calculated band structure of (a) bulk Ag_3PO_4, (b) $Ag_3PO_4(111)$, (c) bulk g-C_3N_4, (d) g-C_3N_4 monolayer and (e) hybrid structure $Ag_3PO_4(111)$/g-C_3N_4.

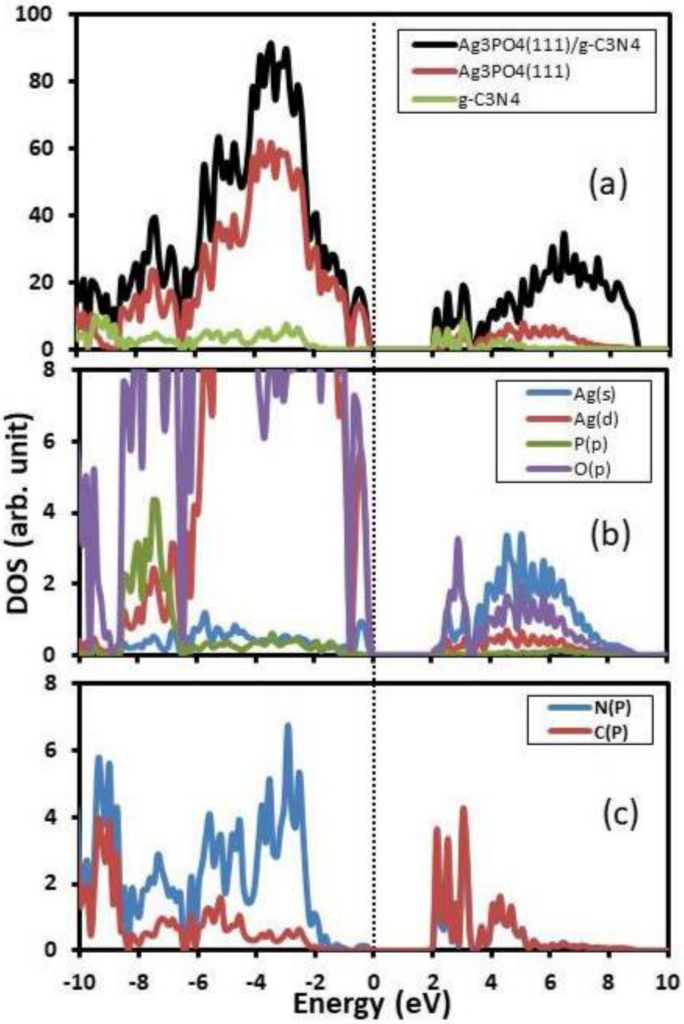

Fig. 4. (a) The calculated TDOS and PDOS of the hybrid $Ag_3PO_4(111)/g\text{-}C_3N_4$. (b) PDOS of $Ag_3PO_4(111)$ in the hybrid $Ag_3PO_4(111)/g\text{-}C_3N_4$. (c) PDOS of $g\text{-}C_3N_4$ in the hybrid $Ag_3PO_4(111)/g\text{-}C_3N_4$.

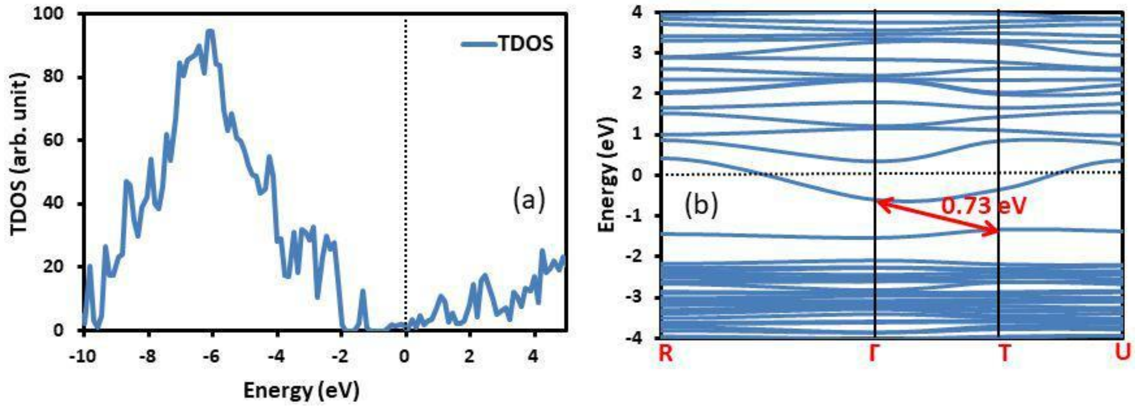

Fig. 5. The calculated (a) TDOS, and (b) band structure of the hybrid $Ag_3PO_4(111)/Ag/g\text{-}C_3N_4$. Energy=0 eV corresponds to the Fermi level.

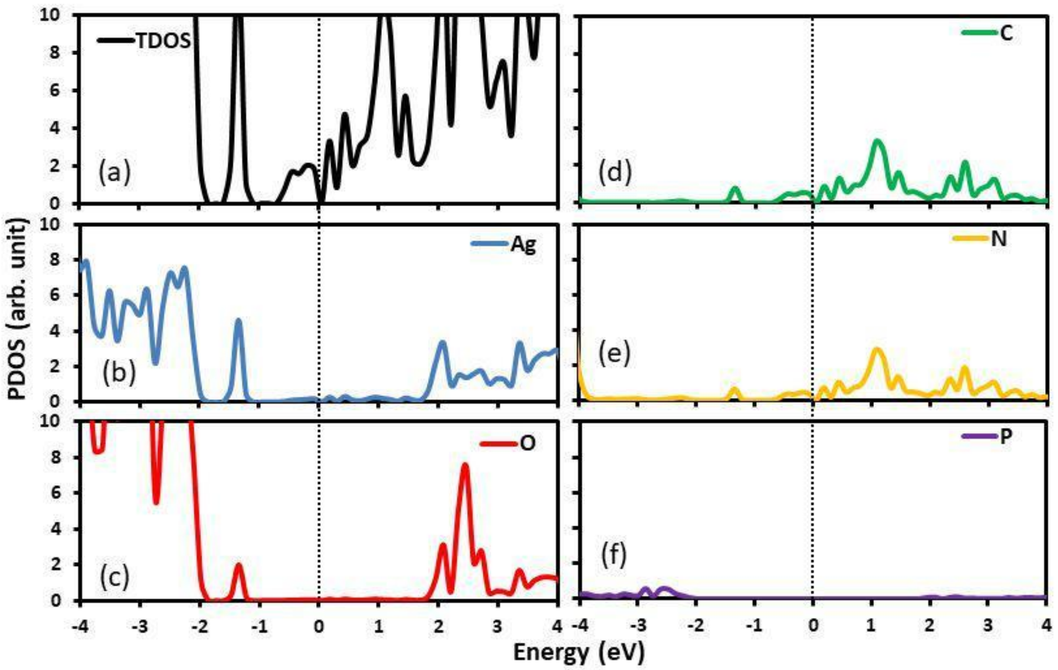

Fig. 6. (a) The calculated TDOS, (b-f) PDOS of the hybrid $Ag_3PO_4(111)/Ag/g\text{-}C_3N_4$. Energy=0 eV corresponds to the Fermi level.

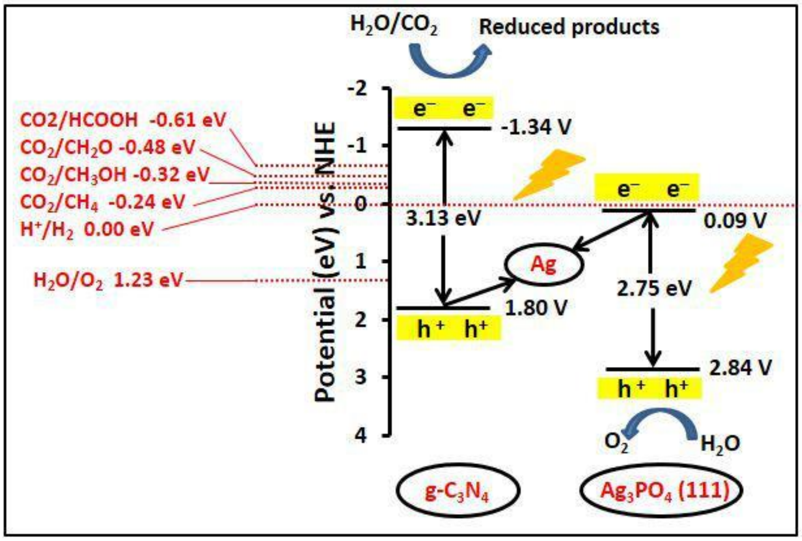

Fig. 7. The calculated Z-scheme charge transfer mechanism of the $Ag_3PO_4(111)/Ag/g\text{-}C_3N_4$ hybrid composite under photoirradiation

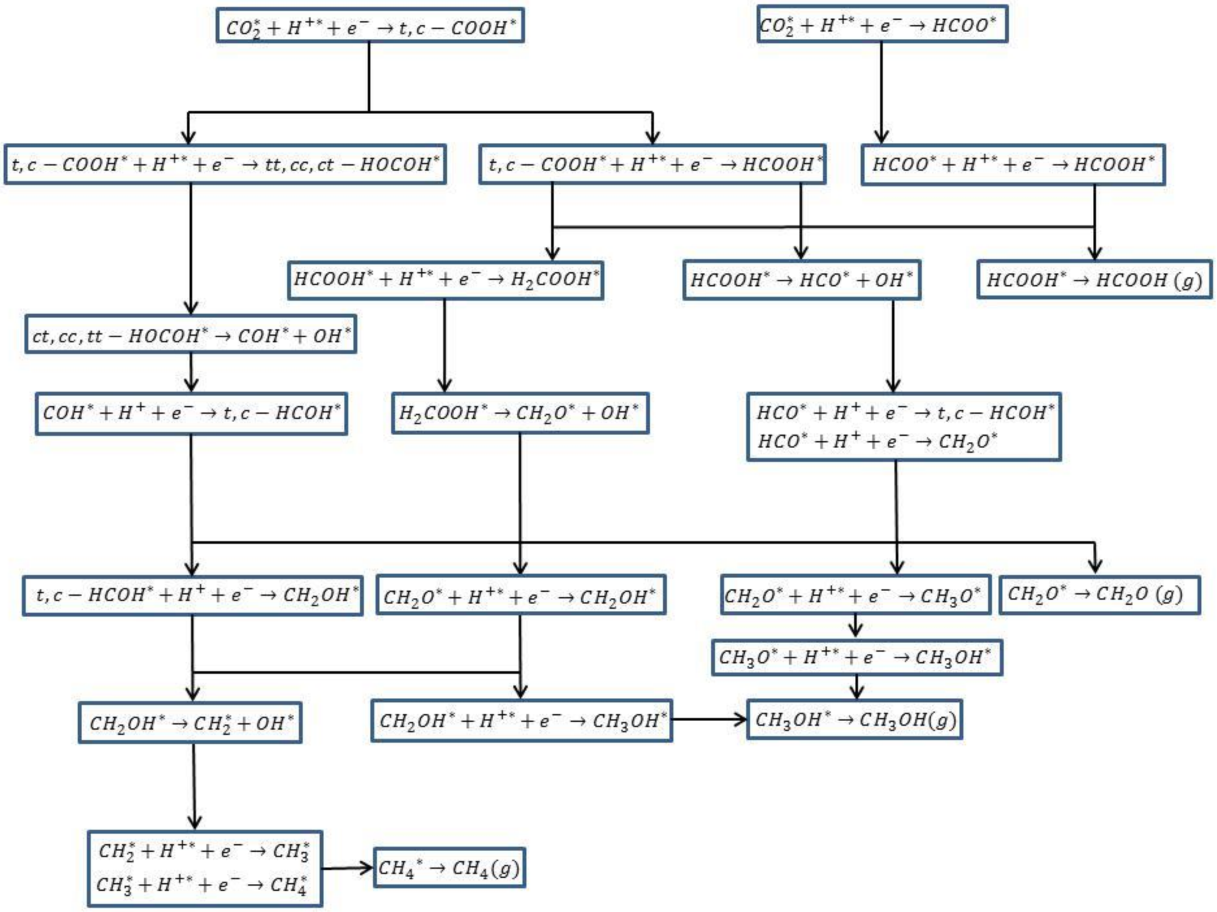

Fig. 8. Possible reaction pathways for CO_2 hydrogenation to form CH_3OH, CH_2O, HCOOH, and CH_4 products.

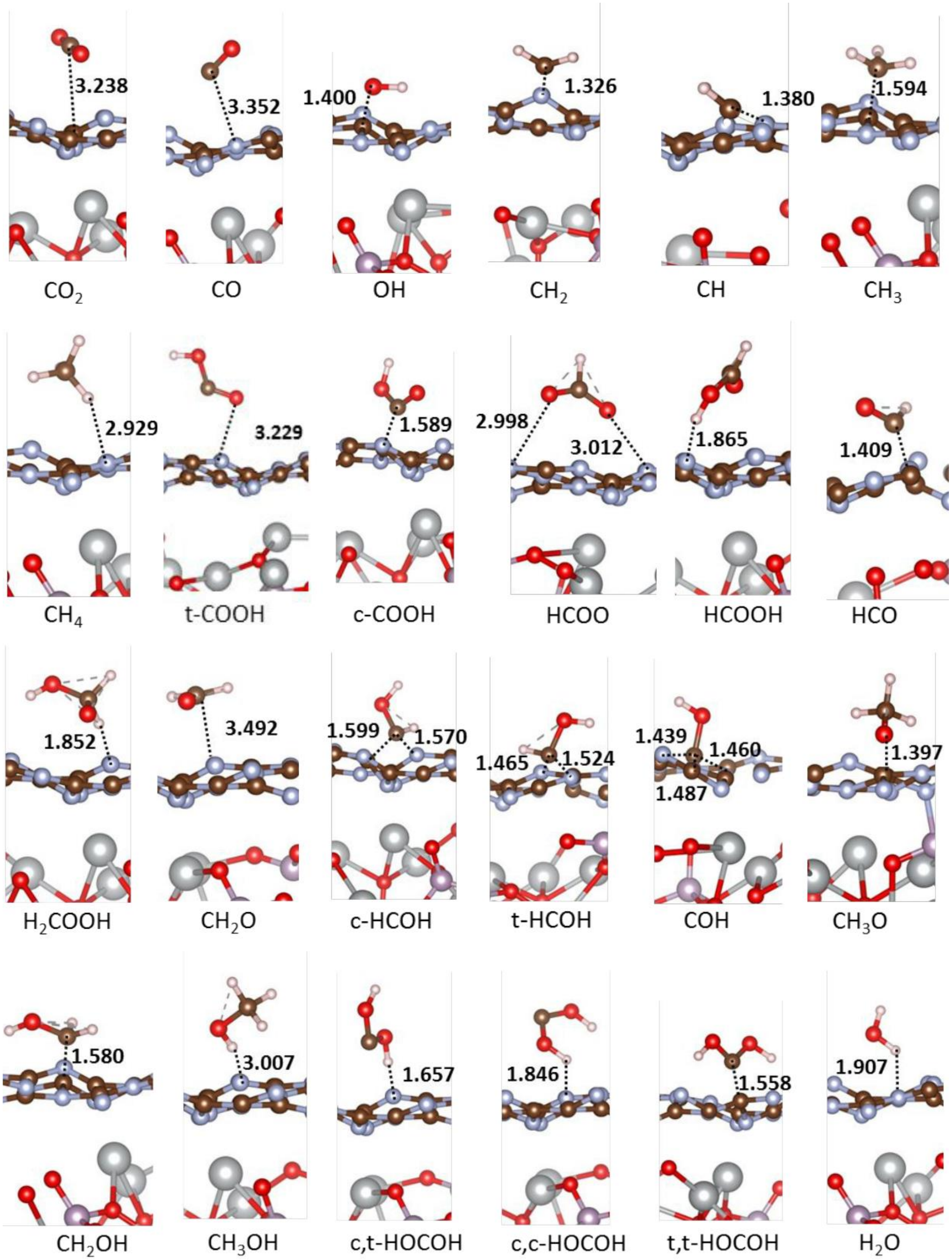

Fig. 9. All possible adsorption geometries of reaction intermediates on the $Ag_3PO_4(111)/g\text{-}C_3N_4$ (All distances are in Å).

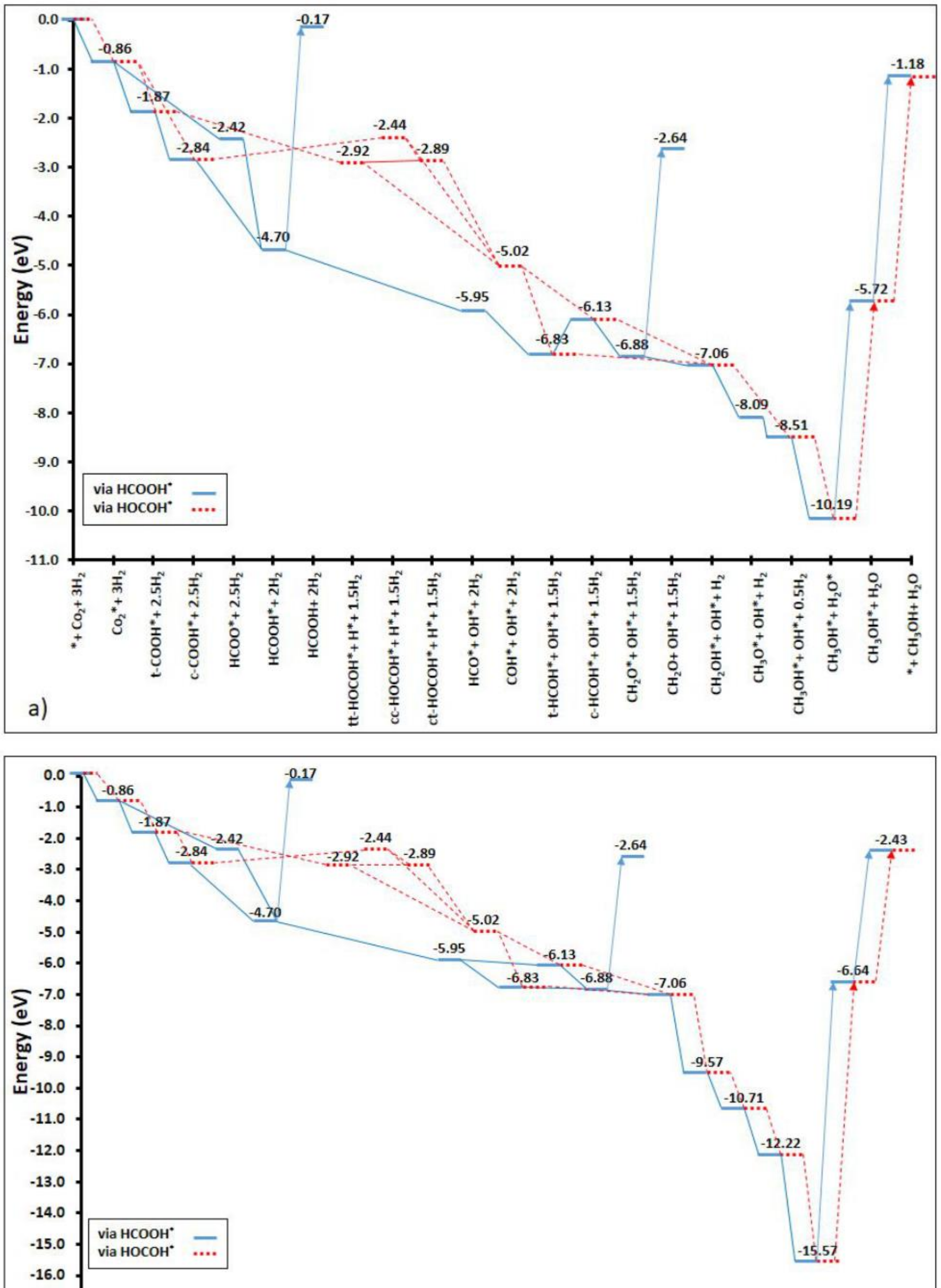

Fig. 10. Reaction profiles for CO_2 and subsequent hydrogenation of intermediates to a) CH_3OH, and b) CH_4 via HOCOH and HCOOH on the Ag_3PO_4(111)/g-C_3N_4 nanocomposite relative to the summation of the total free energy of the photocatalyst, CO_2 and a) three and b) four H_2 in the gas phase. The total energies of + ( ) + − and 1 2 2( ) are considered equal.

Table. 1. Possible reactions in the hydrogenation of intermediates to form CH_3OH, CH_2O, HCOOH, CH_4 products. The calculated reaction energies are reported, where ΔE values of the adsorption and desorption processes are the corresponding E_{ads} and E_{des} values relative to their gas phase, respectively.

Elementary reactions	**ΔE (eV)**
$2(\ ) \rightarrow 2^*$	-0.860
$2^* + {}^{+*} + {}^{-} \rightarrow {}^{*}$	-1.565
$2^* + {}^{+*} + {}^{-} \rightarrow -^*$	-1.014
$2^* + {}^{+*} + {}^{-} \rightarrow -^*$	-1.983
${}^* + {}^{+*} + {}^{-} \rightarrow {}^{*}$	-2.275
$-^* + {}^{+*} + {}^{-} \rightarrow {}^{*}$	-1.857
$-^* + {}^{+*} + {}^{-} \rightarrow {}^{*}$	-2.826
$-^* + {}^{+*} + {}^{-} \rightarrow -^*$	-1.046
$-^* + {}^{+*} + {}^{-} \rightarrow -^*$	-0.050
$-^* + {}^{+*} + {}^{-} \rightarrow -^*$	-1.020
$-^* + {}^{+*} + {}^{-} \rightarrow -^*$	0.408
$-^* \rightarrow -^*$	-0.484
$-^* \rightarrow -^*$	-0.026
${}^* + {}^{+*} + {}^{-} \rightarrow 2^*$	1.898
${}^* \rightarrow {}^* + {}^*$	-1.248
${}^* + {}^{+*} + {}^{-} \rightarrow -^*$	-0.884
${}^* + {}^{+*} + {}^{-} \rightarrow -^*$	-0.182
${}^* + {}^{+*} + {}^{-} \rightarrow 2\ {}^*$	-0.930
$-^* \rightarrow -^*$	-0.702
$2\ {}^* + {}^{+*} + {}^{-} \rightarrow 3$	-1.216
$2\ {}^* + {}^{+*} + {}^{-} \rightarrow 2\ {}^*$	-0.182
$-^* + {}^{*+} + {}^{-} \rightarrow 2\ {}^*$	-0.228
$3\ {}^* + {}^{+*} + {}^{-} \rightarrow 3\ {}^*$	-0.419
$2\ {}^* + {}^{+*} + {}^{-} \rightarrow 3\ {}^*$	-1.453
$2\ {}^* \rightarrow 2^* + {}^*$	-2.511
$2^* + {}^{+*} + {}^{-} \rightarrow 3^*$	-1.141
$3^* + {}^{+*} + {}^{-} \rightarrow 4^*$	-1.508
$-^* \rightarrow {}^* + {}^*$	-2.097
${}^* + {}^{+*} + {}^{-} \rightarrow -^*$	-1.816
${}^* + {}^{+*} + {}^{-} \rightarrow -^*$	-1.114
${}^* \rightarrow (\ )$	4.532
$2\ {}^* \rightarrow 2(\ )$	4.235
$4^* \rightarrow 4(\ )$	4.213
$3\ {}^* \rightarrow 3\ (\ )$	4.544
$2\ {}^* \rightarrow 2(\ )$	4.465

References

1. Nataly Echevarria Huaman, R.; Xiu Jun, T., Energy Related CO$_2$ Emissions and the Progress on CcS Projects: A Review. *Renew. Sust. Energ. Rev.* **2014**, *31*, 368-385.
2. Jiang, Z.; Wan, W.; Li, H.; Yuan, S.; Zhao, H.; Wong, P. K., A Hierarchical Z-Scheme A-Fe$_2$o$_3$/G-C$_3$n$_4$ Hybrid for Enhanced Photocatalytic Co$_2$ Reduction. *Adv. Mater.* **2018**, *30*, 1706108.
3. Ohno, T.; Murakami, N.; Koyanagi, T.; Yang, Y., Photocatalytic Reduction of Co$_2$ over a Hybrid Photocatalyst Composed of Wo$_3$ and Graphitic Carbon Nitride (G-C$_3$n$_4$) under Visible Light. *J. CO$_2$. util.* **2014**, *6*, 17-25.
4. Bi, Y.; Ouyang, S.; Umezawa, N.; Cao, J.; Ye, J., Facet Effect of Single-Crystalline Ag$_3$po$_4$ Sub-Microcrystals on Photocatalytic Properties. *J. Am. Chem. Soc.* **2011**, *133*, 6490-6492.
5. Yi, Z.; Ye, J.; Kikugawa, N.; Kako, T.; Ouyang, S.; Stuart-Williams, H.; Yang, H.; Cao, J.; Luo, W.; Li, Z., et al., An Orthophosphate Semiconductor with Photooxidation Properties under Visible-Light irradiation. *Nat Mater* **2010**, *9*, 559-564.
6. Yao, W.; Zhang, B.; Huang, C.; Ma, C.; Song, X.; Xu, Q., Synthesis and Characterization of High Efficiency and Stable Ag$_3$po$_4$/Tio$_2$ Visible Light Photocatalyst for the Degradation of Methylene Blue and Rhodamine B Solutions. *J. Mater. Chem.* **2012**, *22*, 4050-4055.
7. Dong, C.; Wu, K.-L.; Li, M.-R.; Liu, L.; Wei, X.-W., Synthesis of Ag$_3$po$_4$–Zno Nanorod Composites with High Visible-Light Photocatalytic Activity. *Catal. Commun.* **2014**, *46*, 32-35.
8. Fu, G.; Xu, G.; Chen, S.; Lei, L.; Zhang, M., Ag$_3$po$_4$/Bi$_2$wo$_6$ Hierarchical Heterostructures with Enhanced Visible Light Photocatalytic Activity for the Degradation of Phenol. *Catal. Commun.* **2013**, *40*, 120-124.
9. Cui, Z.; Si, M.; Zheng, Z.; Mi, L.; Fa, W.; Jia, H., Preparation and Characterization of Ag$_3$po$_4$/Bioi Composites with Enhanced Visible Light Driven Photocatalytic Performance. *Catal. Commun.* **2013**, *42*, 121-124.
10. Chen, G.; Sun, M.; Wei, Q.; Zhang, Y.; Zhu, B.; Du, B., Ag$_3$po$_4$/Graphene-Oxide Composite with Remarkably Enhanced Visible-Light-Driven Photocatalytic Activity toward Dyes in Water. *J. Hazard. Mater.* **2013**, *244-245*, 86-93.
11. Dong, P.; Wang, Y.; Cao, B.; Xin, S.; Guo, L.; Zhang, J.; Li, F., Ag$_3$po$_4$/Reduced Graphite Oxide Sheets Nanocomposites with Highly Enhanced Visible Light Photocatalytic Activity and Stability. *Appl. Catal., B* **2013**, *132-133*, 45-53.
12. Zhang, H.; Huang, H.; Ming, H.; Li, H.; Zhang, L.; Liu, Y.; Kang, Z., Carbon Quantum Dots/Ag$_3$po$_4$ Complex Photocatalysts with Enhanced Photocatalytic Activity and Stability under Visible Light. *J. Mater. Chem.* **2012**, *22*, 10501-10506.
13. Faraji, M.; Yousefi, M.; Yousefzadeh, S.; Zirak, M.; Naseri, N.; Jeon, T. H.; Choi, W.; Moshfegh, A. Z., Two-Dimensional Materials in Semiconductor Photoelectrocatalytic Systems for Water Splitting. *Energ. Environ. Sci* **2019**, *12*, 59-95.
14. Yan, S. C.; Li, Z. S.; Zou, Z. G., Photodegradation Performance of G-C$_3$n$_4$ Fabricated by Directly Heating Melamine. *Langmuir* **2009**, *25*, 10397-10401.
15. Naseri, A.; Samadi, M.; Pourjavadi, A.; Moshfegh, A. Z.; Ramakrishna, S., Graphitic Carbon Nitride (G-C$_3$n$_4$)-Based Photocatalysts for Solar Hydrogen Generation: Recent Advances and Future Development Directions. *J. Mater. Chem. A* **2017**, *5*, 23406-23433.
16. Zhu, B.; Zhang, L.; Xu, D.; Cheng, B.; Yu, J., Adsorption Investigation of Co$_2$ on G-C$_3$n$_4$ Surface by Dft Calculation. *J. CO$_2$. util.* **2017**, *21*, 327-335.

17. Zhou, J.; Zhang, M.; Zhu, Y., Photocatalytic Enhancement of Hybrid C_3n_4/Tio_2 Prepared Via Ball Milling Method. *PCCP* **2015**, *17*, 3647-3652.

18. Fu, J.; Chang, B.; Tian, Y.; Xi, F.; Dong, X., Novel C_3n_4-Cds Composite Photocatalysts with Organic-Inorganic Heterojunctions: In Situ Synthesis, Exceptional Activity, High Stability and Photocatalytic Mechanism. *J. Mater. Chem. A* **2013**, *1*, 3083-3090.

19. Hao, Q.; Niu, X.; Nie, C.; Hao, S.; Zou, W.; Ge, J.; Chen, D.; Yao, W., A Highly Efficient G-C_3n_4/Sio_2 Heterojunction: The Role of Sio_2 in the Enhancement of Visible Light Photocatalytic Activity. *PCCP* **2016**, *18*, 31410-31418.

20. Li, F.-t.; Zhao, Y.; Wang, Q.; Wang, X.-j.; Hao, Y.-j.; Liu, R.-h.; Zhao, D., Enhanced Visible-Light Photocatalytic Activity of Active Al_2o_3/G-C_3n_4 Heterojunctions Synthesized Via Surface Hydroxyl Modification. *J. Hazard. Mater.* **2015**, *283*, 371-381.

21. Wu, J.; Shen, X.; Miao, X.; Ji, Z.; Wang, J.; Wang, T.; Liu, M., An All-Solid-State Z-Scheme G-C_3n_4/Ag/Ag_3vo_4 Photocatalyst with Enhanced Visible-Light Photocatalytic Performance. *Eur. J. Inorg. Chem.* **2017**, *2017*, 2845-2853.

22. Yousefi, M.; Faraji, M.; Asgari, R.; Moshfegh, A. Z., Effect of Boron and Phosphorus Codoping on the Electronic and Optical Properties of Graphitic Carbon Nitride Monolayers: First-Principle Simulations. *Phys. Rev. B* **2018**, *97*, 195428.

23. Xiong, T.; Cen, W.; Zhang, Y.; Dong, F., Bridging the G-C_3n_4 Interlayers for Enhanced Photocatalysis. *ACS Catal.* **2016**, *6*, 2462-2472.

24. Cheng, N.; Tian, J.; Liu, Q.; Ge, C.; Qusti, A. H.; Asiri, A. M.; Al-Youbi, A. O.; Sun, X., Au-Nanoparticle-Loaded Graphitic Carbon Nitride Nanosheets: Green Photocatalytic Synthesis and Application toward the Degradation of Organic Pollutants. *ACS Appl. Mater. Interfaces.* **2013**, *5*, 6815-6819.

25. Yang, X.; Chen, Z.; Xu, J.; Tang, H.; Chen, K.; Jiang, Y., Tuning the Morphology of G-C_3n_4 for Improvement of Z-Scheme Photocatalytic Water Oxidation. *ACS Appl. Mater. Interfaces.* **2015**, *7*, 15285-15293.

26. Xiaofei, Y.; Hua, T.; Jingsan, X.; Markus, A.; Menny, S., Silver Phosphate/Graphitic Carbon Nitride as an Efficient Photocatalytic Tandem System for Oxygen Evolution. *ChemSusChem* **2015**, *8*, 1350-1358.

27. Katsumata, H.; Sakai, T.; Suzuki, T.; Kaneco, S., Highly Efficient Photocatalytic Activity of G-C_3n_4/Ag_3po_4 Hybrid Photocatalysts through Z-Scheme Photocatalytic Mechanism under Visible Light. *Ind. Eng. Chem. Res.* **2014**, *53*, 8018-8025.

28. Sun, M.; Zeng, Q.; Zhao, X.; Shao, Y.; Ji, P.; Wang, C.; Yan, T.; Du, B., Fabrication of Novel G-C_3n_4 Nanocrystals Decorated Ag_3po_4 Hybrids: Enhanced Charge Separation and Excellent Visible-Light Driven Photocatalytic Activity. *J. Hazard. Mater.* **2017**, *339*, 9-21.

29. Zhang, F. J.; Xie, F. Z.; Zhu, S. F.; Liu, J.; Zhang, J.; Mei, S. F.; Zhao, W., A Novel Photofunctional G-C_3n_4/Ag_3po_4 Bulk Heterojunction for Decolorization of Rh.B. *Chem. Eng. J.* **2013**, *228*, 435-441.

30. Xu, H.; Zhao, H.; Song, Y.; Yan, W.; Xu, Y.; Li, H.; Huang, L.; Yin, S.; Li, Y.; Zhang, Q., et al., G-C_3n_4/Ag_3po_4 Composites with Synergistic Effect for Increased Photocatalytic Activity under the Visible Light Irradiation. *Mater. Sci. Semicond. Process.* **2015**, *39*, 726-734.

31. Xuxing, C.; Xintang, H.; Zhiguo, Y., Enhanced Ethylene Photodegradation Performance of G-C_3n_4– Ag_3po_4 Composites with Direct Z-Scheme Configuration. *Chem. Eur. J.* **2014**, *20*, 17590-17596.

32. Liu, L.; Qi, Y.; Lu, J.; Lin, S.; An, W.; Liang, Y.; Cui, W., A Stable Ag_3po_4@G-C_3n_4 Hybrid Core@Shell Composite with Enhanced Visible Light Photocatalytic Degradation. *Appl. Catal., B* **2016**, *183*, 133-141.

33. Tang, C.; Liu, E.; Fan, J.; Hu, X.; Ma, Y.; Wan, J., A Graphitic-C_3n_4-Hybridized Ag_3po_4 Tetrahedron with Reactive {111} Facets to Enhance the Visible-Light Photocatalytic Activity. *RSC Adv.* **2015**, *5*, 91979-91987.

34. Zhang, W.; Zhou, L.; Shi, J.; Deng, H., Synthesis of Ag_3po_4/G-C_3n_4 Composite with Enhanced Photocatalytic Performance for the Photodegradation of Diclofenac under Visible Light Irradiation. *Catalysts* **2018**, *8*, 45.

35. Zhou, L.; Zhang, W.; Chen, L.; Deng, H., Z-Scheme Mechanism of Photogenerated Carriers for Hybrid Photocatalyst Ag_3po_4/G-C_3n_4 in Degradation of Sulfamethoxazole. *J. Colloid Interface Sci.* **2017**, *487*, 410-417.

36. He, Y.; Zhang, L.; Teng, B.; Fan, M., New Application of Z-Scheme Ag_3po_4/G-C_3n_4 Composite in Converting Co_2 to Fuel. *Environ. Sci. Technol.* **2015**, *49*, 649-656.

37. Zheng, B.; Wang, X.; Liu, C.; Tan, K.; Xie, Z.; Zheng, L., High-Efficiently Visible Light-Responsive Photocatalysts: Ag_3po_4 Tetrahedral Microcrystals with Exposed {111} Facets of High Surface Energy. *J. Mater. Chem. A* **2013**, *1*, 12635-12640.

38. Martin, D. J.; Umezawa, N.; Chen, X.; Ye, J.; Tang, J., Facet Engineered Ag_3po4 for Efficient Water Photooxidation. *Energ. Environ. Sci* **2013**, *6*, 3380-3386.

39. Martin, D. J.; Liu, G.; Moniz, S. J. A.; Bi, Y.; Beale, A. M.; Ye, J.; Tang, J., Efficient Visible Driven Photocatalyst, Silver Phosphate: Performance, Understanding and Perspective. *Chem. Soc. Rev.* **2015**, *44*, 7808-7828.

40. Kresse, G.; Furthmüller, J., Efficient Iterative Schemes for Ab Initio Total-Energy Calculations Using a Plane-Wave Basis Set. *Phys. Rev. B* **1996**, *54*, 11169-11186.

41. Kresse, G.; Furthmüller, J., Efficiency of Ab-Initio Total Energy Calculations for Metals and Semiconductors Using a Plane-Wave Basis Set. *Comput. Mater. Sci.* **1996**, *6*, 15-50.

42. Perdew, J. P.; Burke, K.; Ernzerhof, M., Generalized Gradient Approximation Made Simple. *Phys Rev Lett* **1996**, *77*, 3865-3868.

43. Kresse, G.; Joubert, D., From Ultrasoft Pseudopotentials to the Projector Augmented-Wave Method. *Phys. Rev. B* **1999**, *59*, 1758-1775.

44. Blochl, P. E., Projector Augmented-Wave Method. *Phys Rev B* **1994**, *50*, 17953-17979.

45. Tafreshi, S. S.; Roldan, A.; de Leeuw, N. H., Density Functional Theory Calculations of the Hydrazine Decomposition Mechanism on the Planar and Stepped Cu(111) Surfaces. *PCCP* **2015**, *17*, 21533-21546.

46. Grimme, S.; Ehrlich, S.; Goerigk, L., Effect of the Damping Function in Dispersion Corrected Density Functional Theory. *J. Comput. Chem.* **2011**, *32*, 1456-1465.

47. Paier, J.; Marsman, M.; Hummer, K.; Kresse, G.; Gerber, I. C.; Ángyán, J. G., Screened Hybrid Density Functionals Applied to Solids. *J. Chem. Phys.* **2006**, *124*, 154709.

48. Paier, J.; Hirschl, R.; Marsman, M.; Kresse, G., The Perdew–Burke–Ernzerhof Exchange-Correlation Functional Applied to the G2-1 Test Set Using a Plane-Wave Basis Set. *J. Chem. Phys.* **2005**, *122*, 234102.

49. Krukau, A. V.; Vydrov, O. A.; Izmaylov, A. F.; Scuseria, G. E., Influence of the Exchange Screening Parameter on the Performance of Screened Hybrid Functionals. *J. Chem. Phys.* **2006**, *125*, 224106.

50. Liu, J.; Cheng, B.; Yu, J., A New Understanding of the Photocatalytic Mechanism of the Direct Z-Scheme G-C_3n_4/Tio_2 Heterostructure. *PCCP* **2016**, *18*, 31175-31183.

51. Ma, X.; Lu, B.; Li, D.; Shi, R.; Pan, C.; Zhu, Y., Origin of Photocatalytic Activation of Silver Orthophosphate from First-Principles. *J. Phys. Chem. C* **2011**, *115*, 4680-4687.

52. Wang, J.; Guan, Z.; Huang, J.; Li, Q.; Yang, J., Enhanced Photocatalytic Mechanism for the Hybrid G-C_3n_4/Mos_2 Nanocomposite. *J. Mater. Chem. A* **2014**, *2*, 7960-7966.

53. Niu, P.; Yang, Y.; Yu, J. C.; Liu, G.; Cheng, H.-M., Switching the Selectivity of the Photoreduction Reaction of Carbon Dioxide by Controlling the Band Structure of a G-C_3n_4 Photocatalyst. *Chem. Commun.* **2014**, *50*, 10837-10840.

54. Monkhorst, H. J.; Pack, J. D., Special Points for Brillouin-Zone Integrations. *Phys Rev B* **1976**, *13*, 5188-5192.

55. Algara-Siller, G.; Severin, N.; Chong, S. Y.; Björkman, T.; Palgrave, R. G.; Laybourn, A.; Antonietti, M.; Khimyak, Y. Z.; Krasheninnikov, A. V.; Rabe, J. P., et al., Triazine-Based Graphitic Carbon Nitride: A Two-Dimensional Semiconductor. *Angewandte Chemie International Edition* **2014**, *53*, 7450-7455.

56. Kahk, J. M.; Sheridan, D. L.; Kehoe, A. B.; Scanlon, D. O.; Morgan, B. J.; Watson, G. W.; Payne, D. J., The Electronic Structure of Silver Orthophosphate: Experiment and Theory. *J. Mater. Chem. A* **2014**, *2*, 6092-6099.

57. Teter, D. M.; Hemley, R. J., Low-Compressibility Carbon Nitrides. *Science* **1996**, *271*, 53-55.

58. Liu, J. J.; Fu, X. L.; Chen, S. F.; Zhu, Y. F., Electronic Structure and Optical Properties of Ag$_3$po$_4$ Photocatalyst Calculated by Hybrid Density Functional Method. *Appl. Phys. Lett.* **2011**, *99*, 191903.

59. Jiang, D.; Zhu, J.; Chen, M.; Xie, J., Highly Efficient Heterojunction Photocatalyst Based on Nanoporous G-C$_3$n$_4$ Sheets Modified by Ag$_3$po$_4$ Nanoparticles: Synthesis and Enhanced Photocatalytic Activity. *J. Colloid Interface Sci.* **2014**, *417*, 115-120.

60. He, P.; Song, L.; Zhang, S.; Wu, X.; Wei, Q., Synthesis of G-C$_3$n$_4$/Ag$_3$po$_4$ Heterojunction with Enhanced Photocatalytic Performance. *Mater. Res. Bull.* **2014**, *51*, 432-437.

61. Kumar, S.; Surendar, T.; Baruah, A.; Shanker, V., Synthesis of a Novel and Stable G-C$_3$n$_4$-Ag$_3$po$_4$ Hybrid Nanocomposite Photocatalyst and Study of the Photocatalytic Activity under Visible Light Irradiation. *J. Mater. Chem. A* **2013**, *1*, 5333-5340.

62. Zhao, Y.-F.; Yang, Y.; Mims, C.; Peden, C. H. F.; Li, J.; Mei, D., Insight into Methanol Synthesis from CO$_2$ Hydrogenation on Cu(111): Complex Reaction Network and the Effects of H$_2$O. *J. Catal.* **2011**, *281*, 199-211.

63. Gong, X.-Q.; Selloni, A.; Vittadini, A., Density Functional Theory Study of Formic Acid Adsorption on Anatase Tio$_2$(001): Geometries, Energetics, and Effects of Coverage, Hydration, and Reconstruction. *J. Phys. Chem. B* **2006**, *110*, 2804-2811.

TOC Graphic

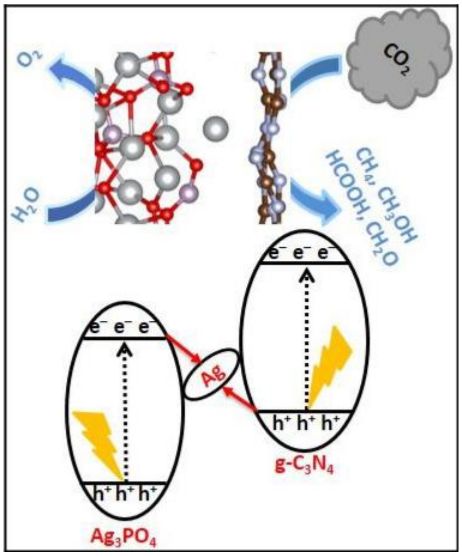
O2
H2O
CO2
CH4, CH3OH
HCOOH, CH2O
e⁻ e⁻ e⁻
h⁺ h⁺ h⁺
Ag
g-C3N4
e⁻ e⁻ e⁻
h⁺ h⁺ h⁺
Ag3PO4